PHYSICAL REVIEW B VOLUME 3, NUMBER 12 15 JUNE 1971

# Lattice Vibrations and Interlayer Interactions in Crystalline $As_2S_3$ and $As_2Se_3$

R. Zallen, M. L. Slade, and A. T. Ward
*Xerox Research Laboratories, Rochester, New York* 14580
(Received 8 January 1971)

Zone-center optical phonons in the layer crystals $As_2S_3$ and $As_2Se_3$ have been investigated in far-infrared reflectivity and transmission measurements (for both polarizations in the layer plane), and in Raman scattering. About a dozen infrared-active fundamentals were found for each crystal, along with a like number of Raman-active modes. Polariton dispersion curves, as well as dielectric dispersion properties and TO and LO frequencies, have been derived from oscillator analyses of the complex reststrahlen spectra. Group-theoretical analysis of the *diperiodic* symmetry of the individual layer, as well as of the triperiodic symmetry of the crystal, reveals that the two symmetries predict experimentally distinguishable lattice optical properties. Our experiments demonstrate the dominance of the layer symmetry. By means of the *combination* of Raman and infrared results, we have been able to observe effects of the weak interlayer interactions; vibrational Davydov splittings have been resolved. A surprisingly simple scaling relation is found to connect the lattice spectra of the two crystals, and these spectra have also been compared to those of the amorphous forms.

## I. INTRODUCTION

### A. General

There are few solids which have been studied in both crystalline and amorphous forms. Among the best-known bulk glasses are the chalcogenides of arsenic, $As_2S_3$ and $As_2Se_3$; considerable work on their optical properties has been reported.[1-3] In contrast to the situation for Ge and Si, for which the crystals are well understood while little is securely known about the amorphous forms, for $As_2S_3$ and $As_2Se_3$ little is known about the crystals. This paper reports an experimental investigation of the lattice vibrations of crystalline $As_2S_3$ and $As_2Se_3$. The one-phonon spectra have been studied in far-infrared reflectivity and transmission measurements (reststrahlen),[4] and in Raman-scattering experiments. Polariton dispersion curves, dielectric dispersion properties, and TO and LO frequencies of the zone-center optical phonons have been derived from the infrared data.

$As_2S_3$ and $As_2Se_3$ crystallize as layer crystals, molecular crystals in which the molecular unit is infinitely extended in two dimensions. In interpreting the observed spectra it is essential to analyze group theoretically the *diperiodic* layer symmetry as well as the triperiodic crystal symmetry: We find that the two symmetries lead to distinctly different photon-phonon selection rules. The fact that the layer and crystal symmetries predict experimentally distinguishable lattice optical properties provides a means to probing the strength of the interaction between layers; we have taken advantage of this fact in this investigation. Our experiments demonstrate the dominance of the layer symmetry. By means of the combination of infrared and Raman spectra, we have been able to observe effects of the weak interlayer interaction; vibrational Davydov splittings have been resolved.

Following the introduction of the structure of the crystals in Sec. IB, the experimentally observed spectra are presented in Sec. II. Experimentally derived dielectric dispersion properties and polariton dispersion curves, as well as TO and LO frequencies of the infrared-active phonons, are obtained from oscillator analyses of the complex reststrahlen spectra (observed for the two polarizations in the layer plane) in Sec. III. The lattice-vibrational consequences of the crystal and layer symmetries, and their interrelationship, are deduced in Sec. IV. The symmetry-determined optical selection rules and the layer-crystal compatibility relations are then applied to the interpretation of the observed Davydov splittings in Sec. VA. In Sec. VB we note a surprisingly simple scaling relation connecting the lattice spectra of the two crystals, and these spectra are compared to those of the glasses. Our principal findings are summarized in Sec. VI.

### B. Orpiment Structure

The structure of orpiment (orpiment is the mineral name for naturally occurring crystalline $As_2S_3$), based on the x-ray work of Morimoto,[5] is shown in Fig. 1. Crystalline $As_2Se_3$ is known to be very closely isomorphic to $As_2S_3$,[6] so that the orpiment structure provides a sound basis for discussing both materials.

These two crystals possess highly pronounced layer structures. Figure 1(a) shows a view of a single layer, looking along the normal to the layer plane. Figure 1(b) shows the 20-atom crystal unit cell, which is two layers thick, with the layers viewed edge on. From the crystallographic data

for $As_2S_3$, the bond length within the layer is 2.24 Å, while the smallest interatomic separation between layers is 3.56 Å, some 59% greater. For $As_2Se_3$ we estimate a value of 1.55 for this ratio of bond lengths. This very large interlayer/intralayer bond-length ratio (1.55–1.59) corresponds to an enormous difference in bond strengths. The very weak bonding between layers is manifested in the outstandingly marked micaceous cleavage exhibited by these crystals. [Their perfect (010) cleavage is, of course, parallel to the layer plane.] For example, these materials can be easily cleaved, using transparent tape, to thicknesses under a micron.[7]

Within the tightly bound layer, each As atom is threefold coordinated and each S (or Se) atom is twofold coordinated. These coordinations are concordant with the covalent bonding requirements of atoms from columns 5 and 6 of the Periodic Table; each needs $8-n$ shared electrons to complete its outermost shell.[8,9] The weak bonding between layers is presumably primarily via van der Waals interactions[10]; Fig. 1(b) indicates that the alignment of adjacent layers is determined largely by packing considerations.

Layer crystals may properly be treated as molecular crystals in which the molecular unit is a sheet infinitely extended in two dimensions. These crystals are network solids in the two directions parallel to the layers and molecular solids in the direction perpendicular to the layers. Graphite, the prototype for all such crystals, is unusually striking in that it is a semimetal in the first two directions and an insulator in the third.[11] While the chalcogenide crystals do not exhibit so dramatic a consequence of the layer structure, they do provide an outstanding opportunity to investigate the relationship between the molecular and the crystalline properties because, as we shall see, the layer and the crystal symmetries are distinct and imply distinctly different optical properties. The experiments reported here exploit this opportunity.

The crystals are of low symmetry, monoclinic, with 20 atoms (4 formula units) in the unit cell. The crystal symmetry is $P2_1/n$ ($C_{2h}^5$), with four operations in the factor group[5,12]:

1, the identity;

$2_b$, a twofold screw axis parallel to the $b$ axis;

$\bar{1}$, inversion through a center of symmetry located midway between layers;

$\bar{2}_b$, a glide plane perpendicular to $b$.

The crystal-symmetry factor-group operations are indicated on Fig. 1(b). Operations $\bar{1}$ and $2_b$ interchange the two layers of the unit cell, while 1 and $\bar{2}_b$ do not. The $b$ axis, the direction along which the layers are stacked (i.e., perpendicular to the layer planes), is the only unique axis of the crystal symmetry; there is nothing to distinquish any direction in the $ac$ (layer) plane from any other.

In the monoclinic unit cell for $C_{2h}$ crystals, the $a$ and $c$ axes are perpendicular to the $b$ axis but may take on any angle with respect to each other. For the axes shown in Fig. 1 the $ac$ angle is, according to Morimoto, $(90.5\pm0.5)^\circ$. If this angle were 90°, the crystal symmetry would remain $P2_1/n$; no new symmetry elements would appear. However, an $ac$ angle of 90° does have a crucial bearing on the *symmetry of each individual isolated layer*, i.e., on the *molecular symmetry*. If we take the $ac$ angle to be 90° and adjust a few atomic coordinates by about 0.02 Å, both assumptions being within the reported crystallographic experimental errors, then we obtain the diperiodic symmetry described below and analyzed group theoretically in Sec. IV B. The diperiodic symmetry of the molecular layer of the orpiment structure has not been previously noted or analyzed.

The factor group for the layer symmetry consists of four operations: two in common with the crystal factor group, and two new ones. The two crystal-symmetry operations are those which transform each layer into itself, the identity 1 and the glide plane $\bar{2}_b$. The two different operations are illustrated on Fig. 1(a):

$2_c$, a twofold screw axis parallel to the $c$ axis;

$\bar{2}_a$, a mirror plane perpendicular to the $a$ axis.

The four operations of the layer symmetry comprise an orthorhombic system in which the $c$ and $a$ axes, as well as the $b$ axis, are axes of symmetry. The space group is $Pnm2_1$; it is, as discussed in Sec. IV B, one of the 80 diperiodic space groups in three dimensions.

Within the 20-atom crystal unit cell there are five inequivalent atomic sites unrelated by symmetry to one another, two As and three S sites. For the 10-atom layer unit cell there are three inequivalent sites, one As and two S. All four unit-cell As atoms are connected by the layer factor-group operations, while the six S atoms divide into four which lie on no symmetry elements and two which lie on the $\bar{2}_a$ mirror plane.

An important feature of the orpiment structure is that the symmetry axes of the layers are parallel. This means that *the molecular symmetry is accessible to experiment*. In many molecular crystals, such as orthorhombic sulfur,[13] there are two or more skewed molecular orientations within the unit cell, so that it is not possible to optically probe the molecular-symmetry selection rules. The parallel orientations of axes $a$, $b$, and $c$ for the two unit-cell layers provide us with a means of investigating molecular aspects of crystalline $As_2S_3$

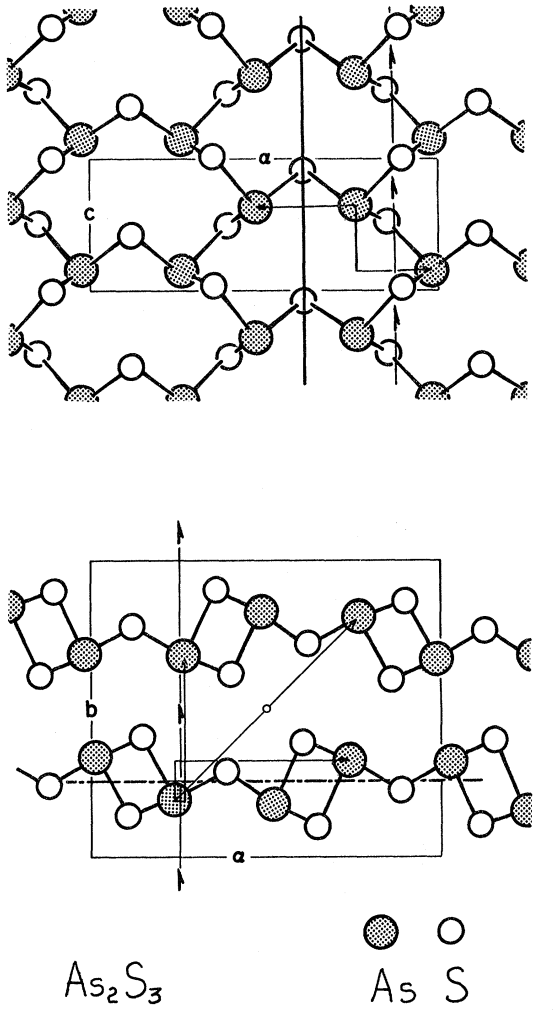


FIG. 1. Crystal structure of $As_2S_3$ and $As_2Se_3$, the orpiment structure. The bottom diagram shows a view along the $c$ axis, looking at the layers edge on; the top diagram shows a view along the $b$ axis, looking down on a single layer. Crystal-symmetry operations are indicated on the former, layer-symmetry operations on the latter.

and $As_2Se_3$.

## II. INFRARED AND RAMAN SPECTRA

### A. Experimental Techniques

Far-infrared reflectivity and transmission measurements were performed with a Perkin-Elmer 301 spectrometer, an instrument employing grating dispersion and an optical path purged with $N_2$ gas. The light source was a globar or a Hg arc, the detector a thermocouple or a Golay cell, depending upon spectral region. The spectrometer was operated single beam, reflected (or transmitted) light intensity being measured in alternate scans of the sample and an Al mirror (or blank aperture). Transmission was measured at normal incidence, reflectivity at an angle of incidence of 9°. A wire grid was used for obtaining polarized light.

For the Raman-scattering experiments, the exciting radiation was supplied by either a cw 100-mW He-Ne gas laser ($h\nu_L = 1.96$ eV) or a cw 10-W YAG : $Nd^{3+}$ (yttrium aluminum garnet) glass laser ($h\nu_L = 1.16$ eV). A Spex 1400 grating double monochromator, with the illuminated part of the sample focused on the entrance slit and a photomultiplier detector located behind the exit slit, was used to analyze the scattered beam. The scattering geometries employed are described in Sec. II B in conjunction with the observed spectra.

Phase-sensitive detection was utilized for all of the measurements: at 13 cps for the infrared experiments, and at 640 cps for the Raman experiments.

Natural crystals of $As_2S_3$, and two types of synthetic $As_2Se_3$ crystals, were used in this study. Large samples of orpiment, originating from the vicinity of Winnemucca, Nev.,[14] yielded transparent yellow $As_2S_3$ crystals (the room-temperature absorption edge of crystalline $As_2S_3$ is 2.5 eV) with facial areas of a few $cm^2$. Because of the pronounced micaceous cleavage, the optically suitable surfaces were restricted to the (010) orientation parallel to the cleavage plane, the plane of the tightly bound layer. For this reason, in our experiments the incident beam was directed along or close to the $b$ axis, with the electric field of the light wave polarized parallel to the layer plane. [The unavoidable (010) cleavage necessarily relegated the inaccessible $E \parallel b$ absorption spectrum to a future investigation involving measurements at oblique incidence.] Reflectivity measurements were made on cleaved surfaces, and transmission measurements were made on a thin sample ($d = 21$ $\mu$, determined by interference fringe spacings) prepared by transparent-tape cleaving. The $As_2S_3$ crystals were of good optical quality, and they were surprisingly pure: Emission spectroscopy uncovered no impurities in concentrations above a few ppm.

The two varieties of synthetic $As_2Se_3$ crystals investigated were prepared by Keezer, Vernon, and Griffiths of the Xerox Research Laboratories. Large ($2 \times 1 \times 0.5$ $cm^3$) nearly-single-crystal ingots, obtained by the vertical Bridgman technique from a thallium-doped melt, provided samples of sufficient size for the infrared reflectivity measurements. This material consisted of lamellar crystals of parallel orientation, and contained a small amount (2%) of a selenium-rich phase as veinous inclusions. Cleaved melt-grown samples were used for the reflectivity studies.

Small single-crystal plates of $As_2Se_3$ were also prepared by our above-mentioned colleagues by

deposition from the vapor. The vapor-grown plates, the largest of which measured $0.8\times0.2\times0.01$ cm$^3$, were of much finer optical quality than the fibrous melt-grown material. Vapor-grown samples were used for the Raman-scattering experiments and (by mounting three plates of parallel orientation over one aperture) also for measurements of infrared transmission.

X-ray fluorescence and electron microprobe measurements revealed the natural $As_2S_3$ crystals, the vapor-grown $As_2Se_3$ crystals, and the crystalline matrix of the melt-grown $As_2Se_3$ samples to be stoichiometric to within the experimental uncertainty of 0.5%

### B. Observed Spectra

In this section we present the experimental results, for subsequent discussion. The near-normal-incidence far-infrared reflectivity spectra of crystalline $As_2S_3$ and $As_2Se_3$ are shown in Figs. 2 and 3. The reststrahlen spectra have been obtained for two of the three principal directions of polarization of these optically biaxial crystals: $E \parallel c$ and $E \parallel a$. (The third independent polarization $E \parallel b$ awaits experiments at oblique incidence.) The points in Figs. 2 and 3 are the experimental

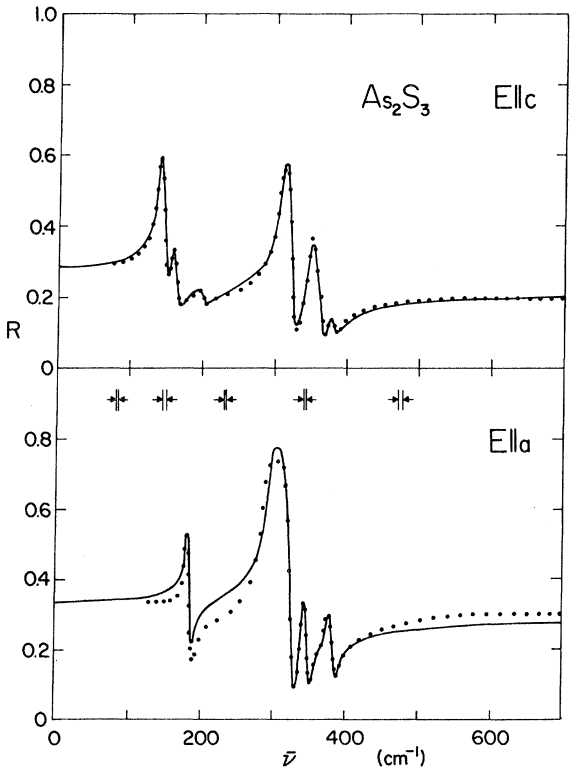


FIG. 2. Reststrahlen spectra for crystalline $As_2S_3$. The points are the experimental data; the curves are the theoretical fits discussed in the text. The arrows and vertical bars indicate instrumental spectral slit widths.

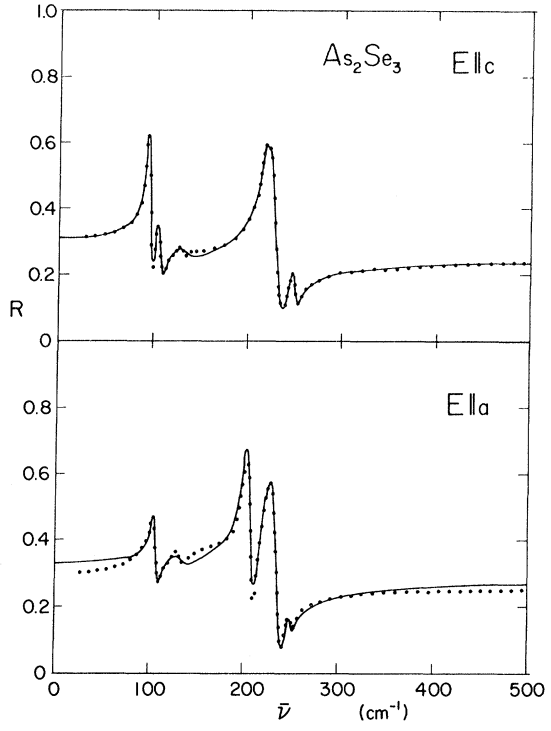


FIG. 3. Reststrahlen spectra for crystalline $As_2Se_3$.

results; the curves are oscillator-analysis theoretical fits discussed in Sec. III A.

Twenty reststrahlen bands are exhibited by the four spectra shown in Figs. 2 and 3. The oscillator strengths and eigenfrequencies for these bands are discussed in Sec. III, along with the deduced dielectric dispersion properties in the infrared. Six additional weaker absorption bands were observed in infrared transmission measurements; their eigenfrequencies are also discussed in Sec. III.

Raman-scattering data for both crystals are displayed in Fig. 4. Scattering intensity is shown plotted against frequency shift from the laser line. Throughout this paper, phonon frequency $\nu$ and photon energy $h\nu$ are expressed in the units of their wave-number equivalent ($\bar{\nu} = \nu/c = h\nu/hc$). The YAG: $Nd^{3+}$ laser was used for $As_2Se_3$ ($\bar{\nu}_L = 0.94\times10^4$ cm$^{-1}$, $\bar{\nu}_G = 1.5\times10^4$ cm$^{-1}$, where $\bar{\nu}_L$ is the laser photon energy in wave-number units and $\bar{\nu}_G$ is the wave-number equivalent of the room-temperature band gap[15–17]). The He-Ne laser was used for $As_2S_3$ ($\bar{\nu}_L = 1.58\times10^4$ cm$^{-1}$, $\bar{\nu}_G = 2.2\times10^4$ cm$^{-1}$ [15]). In each case the laser frequency was substantially below the interband absorption threshold, well within the transparent regime for the crystal. Figure 4 contains both the Stokes (downshifted via phonon emission) and anti-Stokes (upshifted via phonon absorption) scattering spectrum for each crystal. These survey spectra were taken with no polarizer

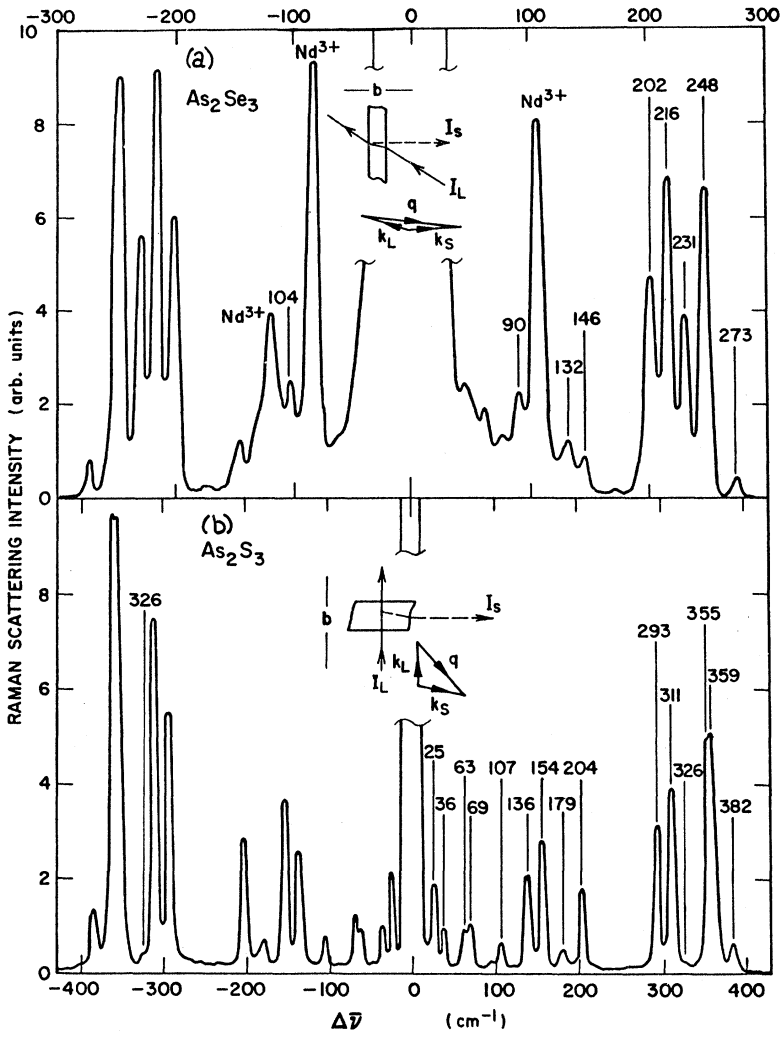


FIG. 4. Raman-scattering spectra for crystalline $As_2Se_3$ and $As_2S_3$. Both Stokes ($\Delta\bar{\nu} < 0$) and anti-Stokes ($\Delta\bar{\nu} > 0$) spectra are shown. A YAG : $Nd^{3+}$ laser was used for $As_2Se_3$, He-Ne laser for $As_2S_3$; the experimental scattering geometries are shown in the inserts.

in incident or scattered beam, in order to expose as many Raman-active modes as possible. The different horizontal scales were chosen to reveal the similarities in the spectra, particularly between the groups of strong lines at 200–250 $cm^{-1}$ for $As_2Se_3$ and at 300–350 $cm^{-1}$ for $As_2S_3$. The scaling factor will be discussed in Sec. V, along with a tabulation of the observed frequencies. Fifteen Raman lines were located for $As_2S_3$ and nine for $As_2Se_3$.

The inserts in Fig. 4 indicate the scattering geometry applicable to each spectrum. In each experiment, the propagation direction of the laser beam inside the crystal was approximately along the $b$ axis. For the thin $As_2Se_3$ platelets and $As_2S_3$ crystals investigated, the geometry was necessarily a backscattering arrangement, as shown in Fig. 4(a). For several thick $As_2S_3$ crystals it was possible to employ right-angle scattering, as indicated in Fig. 4(b).

Using two fine large $As_2S_3$ crystals, we successfully obtained polarization-dependent Raman spectra; several such spectra are displayed in Fig. 5. These spectra, along with the selection rules de-

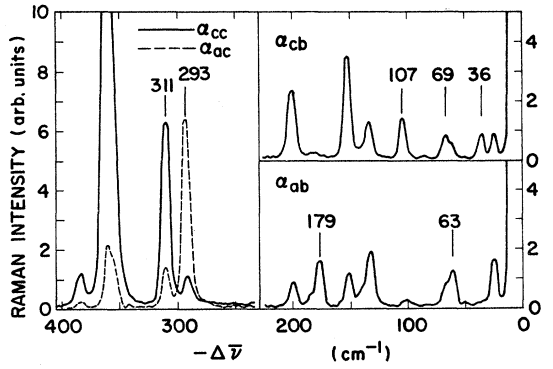


FIG. 5. Polarization-dependent Raman spectra for crystalline $As_2S_3$. The polarizations of incident and scattered beams correspond to the subscripts of the scattering-tensor components used to label the spectra.

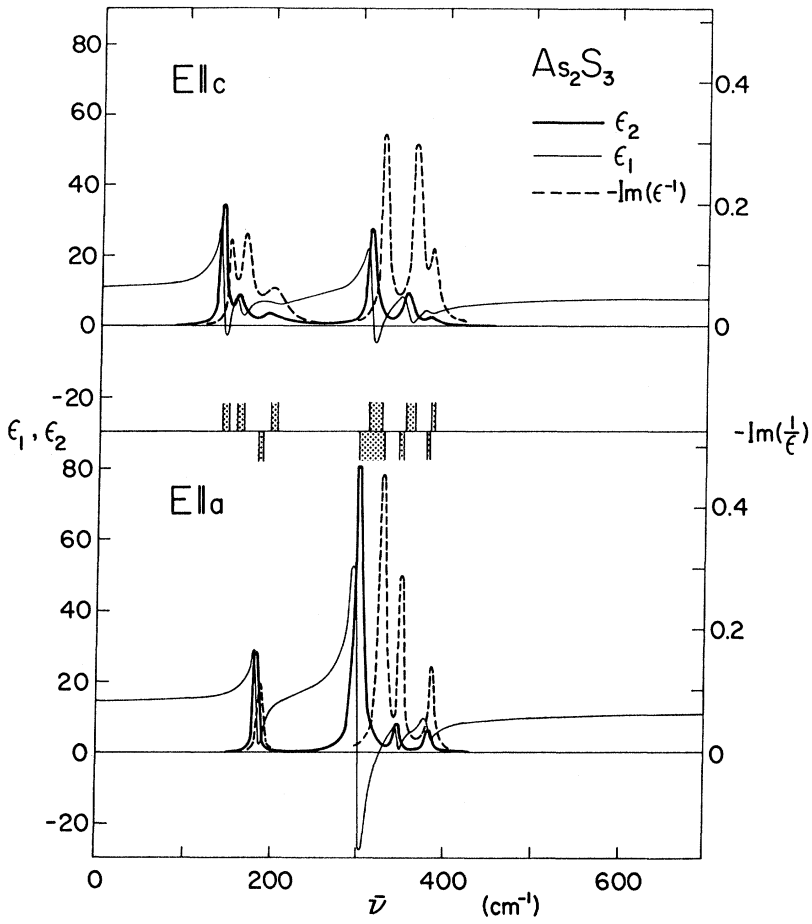


FIG. 6. Dielectric dispersion properties of crystalline $As_2S_3$: $\epsilon_1$ and $\epsilon_2$ are the real and imaginary parts of the dielectric constant; $-\mathrm{Im}(\epsilon^{-1})$ is the energy-loss function.

rived in Sec. IV, are used to determine symmetry assignments for the Raman-active vibrations in Sec. V.

Unlike the reflectivity data, for which the detailed dispersion analysis of Sec. III is required for the derivation of eigenfrequencies, the Raman-scattering data can be treated directly as line spectra. All of the Raman-active eigenfrequencies we observed are given in Fig. 4, and need not be tabulated separately. The peak positions are determined to an accuracy of $\pm 1$ cm$^{-1}$. Aside from the relevance of their polarization dependence (Fig. 5) to selection rules and symmetry assignments, relative Raman-line intensities will not come in for detailed scrutiny here. The important implications of the Raman data will be discussed in Sec. V, in which the Raman and infrared results are combined to yield estimates of intermolecular-interaction splittings.

## III. DISPERSION SPECTRA

### A. Dielectric Dispersion Properties

Dielectric dispersion properties in the far infrared were deduced from the reststrahlen spectra by synthesizing the observed reflectivity with a complex dielectric constant $\epsilon = \epsilon_1 - i\epsilon_2$ constructed as a superposition of Lorentzians:

$$\epsilon(\bar{\nu}) = \epsilon_\infty + \sum_j \frac{s_j \bar{\nu}_j^2}{\bar{\nu}_j^2 - \bar{\nu}^2 + i\gamma_j \bar{\nu}_j \bar{\nu}} \ .$$

$\bar{\nu}_j$, $s_j$, and $\gamma_j$ are the oscillator frequency (in wavenumber units), oscillator strength (contribution to the static dielectric constant), and dimensionless damping constant, respectively, for oscillator $j$, and $\epsilon_\infty$ is the high-frequency dielectric constant. The reflectivity fits are the curves of Figs. 2 and 3; the corresponding $\epsilon$'s are displayed in Figs. 6 and 7. The oscillator parameters, which epitomize the results of the reflectivity measurements, are given in Tables I and II. The oscillator fits were arrived at by means of a computer program which performs an iterative search in parameter space, the optimization criterion being the minimization of the rms deviation of the fitted from the measured reflectivity. Initial parameters for the search were selected by examining the results of a Kramers-Kronig analysis of the data. The tabulated

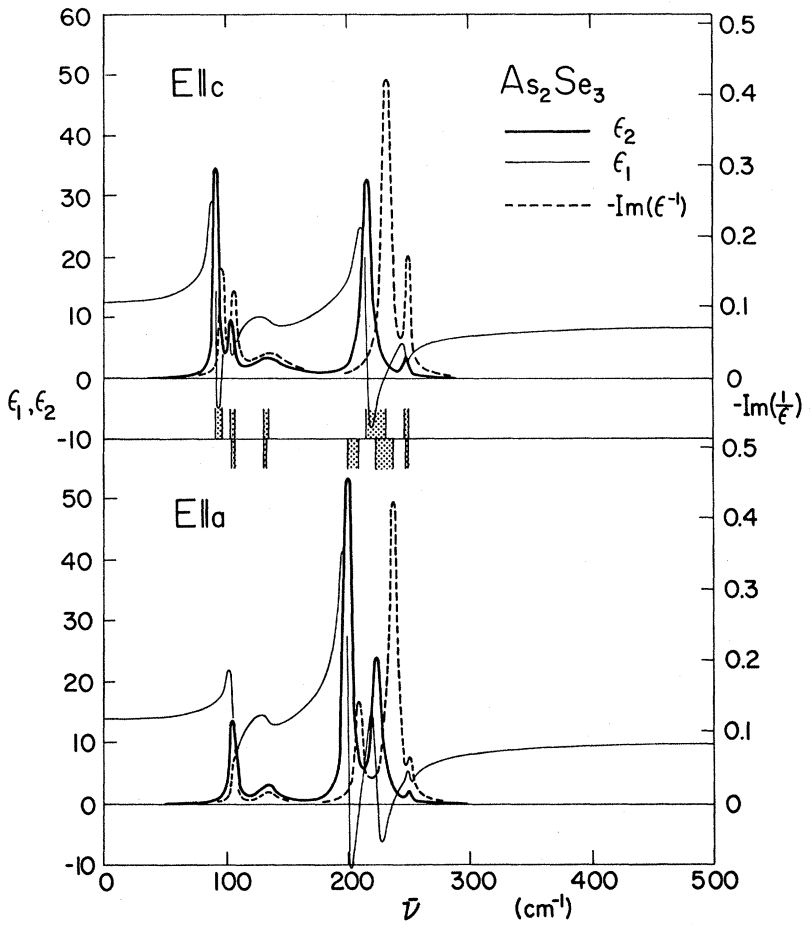


FIG. 7. Dielectric dispersion of crystalline $As_2Se_3$: $\epsilon_1$ and $\epsilon_2$ are the real and imaginary parts of the dielectric constant; $-\mathrm{Im}(\epsilon^{-1})$ is the energy-loss function.

parameters yield fits with values of $\Delta R_{\mathrm{rms}}$ of 0.014, 0.043, 0.009, and 0.021 for the spectra of $As_2S_3$ ($E \parallel c$), $As_2S_3$ ($E \parallel a$), $As_2Se_3$ ($E \parallel c$), and $As_2Se_3$ ($E \parallel a$), respectively.

The $\bar{\nu}_j$'s listed without corresponding $s_j$'s and $\gamma_j$'s are additional infrared-active eigenfrequencies not discernible in reflectivity, but observed as weak absorption bands in infrared transmission. The location of the absorption maxima for the stronger reststrahlen bands, observed in transmission as well as reflectivity, were used to slightly modify (by averaging, with greater weight on the transmission $\bar{\nu}$'s) the $\bar{\nu}_j$'s of the oscillator fits to yield the frequencies of Tables I and II. The accuracy of the infrared eigenfrequencies is estimated as $\pm 2$ cm$^{-1}$.

In Figs. 6 and 7 the positions of the peaks in $\epsilon_2$ locate the frequencies of the $q \approx 0$ [18] transverse-optical (TO) phonons. Also plotted in the figures is the energy-loss function $-\mathrm{Im}(\epsilon^{-1})$ which peaks at the longitudinal-optical (LO) phonon frequencies. (The zeros of $\epsilon_1$ cannot be used to determine the LO frequencies because of the finite damping, which prevents $\epsilon_1$ from being driven negative for all but the strongest bands.) TO and LO frequencies are indicated by the bar graphs along the midlines of Figs. 6 and 7. The barred frequency regimes, bounded above and below by LO and TO frequencies, respectively, signify forbidden zones for long-wavelength phonons (frequency regimes in which there are no propagating waves).

The complex refractive index $n^c = n - ik$ is computationally intermediate between the microscopic variable $\epsilon$ and the observed quantity $R$:

$$\epsilon \to n^c, \quad n^2 = \tfrac{1}{2}\epsilon_1 + \tfrac{1}{2}(\epsilon_1^2 + \epsilon_2^2)^{1/2},$$

$$k^2 = -\tfrac{1}{2}\epsilon_1 + \tfrac{1}{2}(\epsilon_1^2 + \epsilon_2^2)^{1/2};$$

$$n^c \to R, \quad R = [(n-1)^2 + k^2][(n+1)^2 + k^2]^{-1}.$$

Our results for the refractive indices are shown in Figs. 8 and 9.

For $As_2S_3$, our high-frequency values of $n$ ($= \epsilon_\infty^{1/2}$) can be compared to the accurate near-infrared values of Evans and Young[7]: The oscillator results are $n_c = 2.7$ and $n_a = 3.3$, compared with EY's $n_c$

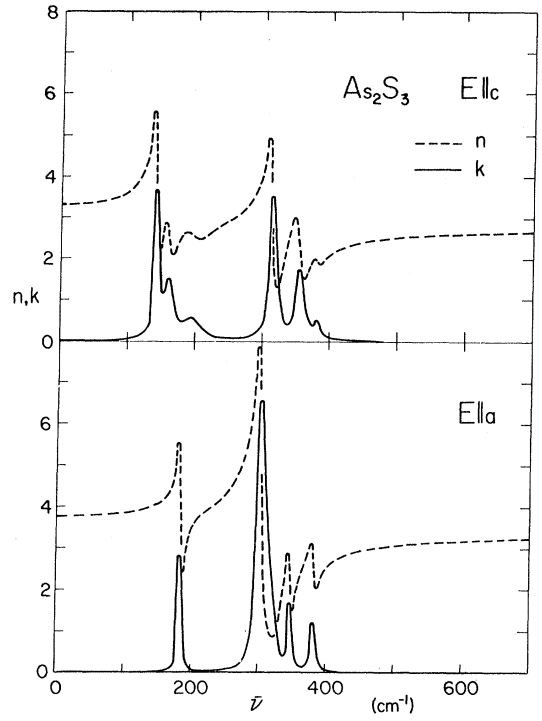


FIG. 8. Complex refractive index of crystalline $As_2S_3$.

$= 2.6$ and $n_a = 3.0$, indicating that our $R_\infty$'s are overestimated by 0.02–0.03.

Tables I and II reveal that, for both crystals, the lattice (infrared) contribution to the static dielectric constant $\epsilon_0$ is smaller than the electronic (ultraviolet) contribution. The phonon contribution to $\epsilon_0$ is $\epsilon_0 - \epsilon_\infty$; the interband contribution is $\epsilon_\infty - 1$. For the four sets of data in the two tables, $(\epsilon_0 - \epsilon_\infty)/(\epsilon_\infty - 1) \approx 0.3$–$0.6$. The phonon contribution itself is about the same (i.e., within experimental error) for both $As_2S_3$ and $As_2Se_3$: $\epsilon_0 - \epsilon_\infty = 3.3$–$3.6$.

### B. Polariton Dispersion Curves

In addition to the reststrahlen-derived dielectric properties of Sec. III A, an important, physically significant, graphical representation of these data is in the form of polariton[19,20] (coupled photon-phonon) dispersion curves. Using a complex propagation vector $q = q_1 + iq_2$ to describe the coupled wave, the wave-number dependence of $q$ is given by $q(\bar{\nu}) = (\omega/c)n^c(\bar{\nu}) = 2\pi\bar{\nu}n^c(\bar{\nu})$. With this expression, along with the $n^c$'s of Figs. 8 and 9, we obtain the dispersion curves of Figs. 10–13. Figures 10 and 11 show dispersion curves for $E \parallel c$ (with $q \parallel b$) and $E \parallel a$ (with $q \parallel b$), respectively, for $As_2S_3$; Figs. 12 and 13 show the corresponding results for $As_2Se_3$.

The solid curves in Figs. 10–13 are the experimentally defined polariton dispersion curves; they correspond to the fitted oscillator parameters of Tables I and II. Letting the damping constants go to zero, we obtain the dashed curves shown in the figures, which display the classical coupled-wave form.[19] The $q = 0$ intercepts of the zero-damping curves locate the LO frequencies; the $q \to 0$ asymptotes determine the TO frequencies. For these curves, the spectral regions in which $q$ is purely imaginary (each of which is bounded above and below by an LO and a TO frequency) correspond to the stopping bands which were indicated by the bars on Figs. 6 and 7.

The upper and lower sloping lines on Figs. 10–13

TABLE I. Oscillator parameters for $As_2S_3$.

| | $\bar{\nu}_t$ (cm$^{-1}$) | $s = \Delta\epsilon_1$ | $\gamma$ |
|---|---|---|---|
| | | $\epsilon_\infty = 7.3$ | |
| $E \parallel c$ | 383 | 0.04 | 0.03 |
| | 354 | 0.3 | 0.03 |
| | 311 | 0.8 | 0.03 |
| | 278 | ••• | ••• |
| | 198 | 0.5 | 0.17 |
| | 159 | 0.5 | 0.08 |
| | 140 | 1.5 | 0.05 |
| | | $\epsilon_0 = 10.9$ | |
| | | $\epsilon_0 = 11.0$ | |
| $E \parallel a$ | 375 | 0.1 | 0.02 |
| | 345 | 0.1 | 0.01 |
| | 299 | 2.4 | 0.03 |
| | 279 | ••• | ••• |
| | 244 | ••• | ••• |
| | 181 | 0.7 | 0.03 |
| | | $\epsilon_0 = 14.3$ | |

TABLE II. Oscillator parameters for $As_2Se_3$.

| | $\bar{\nu}_t$ (cm$^{-1}$) | $s = \Delta\epsilon_1$ | $\gamma$ |
|---|---|---|---|
| | | $\epsilon_\infty = 8.8$ | |
| $E \parallel c$ | 268 | ••• | ••• |
| | 248 | 0.1 | 0.02 |
| | 217 | 1.3 | 0.04 |
| | 132 | 0.6 | 0.24 |
| | 105 | 0.4 | 0.05 |
| | 94 | 1.2 | 0.03 |
| | | $\epsilon_0 = 12.4$ | |
| | | $\epsilon_\infty = 10.5$ | |
| $E \parallel a$ | 287 | ••• | ••• |
| | 266 | ••• | ••• |
| | 249 | 0.01 | 0.01 |
| | 224 | 0.9 | 0.04 |
| | 201 | 1.5 | 0.03 |
| | 132 | 0.4 | 0.14 |
| | 106 | 0.6 | 0.04 |
| | | $\epsilon_0 = 13.9$ | |

correspond, respectively, to the high- and low-frequency behavior of $\bar{\nu}(q)$, and possess slopes inversely proportional to the optical and static refractive indices. The decrease in slope between high and low frequencies reflects the increase in $n$ on passing through the reststrahlen region $n_0 = n_\infty + \int_{\text{lattice bands}} \alpha\, d\lambda$. Without photon-phonon interaction the dispersion curves would reduce to horizontal lines at the frequencies of the pure lattice curves and to the upper straight line representing the undisturbed light waves.

### C. TO and LO Frequencies; Effective Charges

At this juncture we take inventory of the transverse and longitudinal frequencies of the infrared-active $q \approx 0$ phonons, as revealed by our reflectivity and transmission experiments. The resulting catalogs constitute Tables III and IV. The LO frequencies listed are obtained by adding TO-LO splittings, deduced from the polariton dispersion curves, to the TO frequencies of Tables I and II. The TO-LO splittings $(\bar{\nu}_l - \bar{\nu}_t)$ are derived from the zero-damping curves of Figs. 10–13; they are the differences between the $q = 0$ and $q \to \infty$ frequency intercepts for each reststrahlen band. These splittings are also specified by the differences between corresponding maxima of $-\mathrm{Im}(\epsilon^{-1})$ and $\epsilon_2$ in Figs. 6 and 7.

The third column of Tables III and IV contains values of the ionic plasma frequency $\bar{\nu}_p$, defined by $\bar{\nu}_p^2 = s\bar{\nu}_t^2/\epsilon_\infty$. Like $\bar{\nu}_l - \bar{\nu}_t$, $\bar{\nu}_p$ is a frequency measure of oscillator strength. For a simple lattice spectrum containing a single reststrahlen band, the TO, LO, and ionic plasma frequencies are simply related by $\bar{\nu}_l^2 = \bar{\nu}_t^2 + \bar{\nu}_p^2$. With many bands present, as for these complex crystals, the contributions to $\epsilon$ superimpose to shift the locations of the zeros; the LO frequencies are downshifted for the low-frequency bands and upshifted for the high-frequency bands. Values of $(\bar{\nu}_t^2 + \bar{\nu}_p^2)^{1/2}$ are shown in the fourth column of the tables, for comparison with the observed LO frequencies; the many-band shifts are quite small.

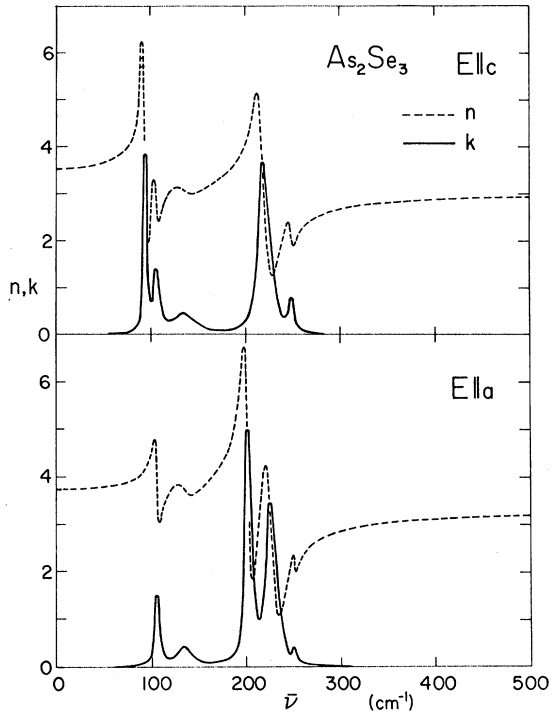


FIG. 9. Complex refractive index of crystalline $As_2Se_3$.

Effective charge is a tensor quantity governing the linear relation between the macroscopic polarization and the unit-cell atomic displacements. For a complex crystal, the problem of determining this quantity from the experimental reststrahlen strengths requires a prior determination of the infrared-active vibrational eigenvectors. Since this information is rarely available, a set of assumptions must usually be invoked in order to estimate effective charges. Such an analysis has been recently reported by Zallen *et al.* for a crystal with a six-atom unit cell.[20] Following arguments similar to theirs, we are led to assume that the largest TO-LO splitting for each polarization corresponds

TABLE III. TO, LO, and ionic plasma frequencies ($\bar{\nu}$ in cm$^{-1}$), and effective charges, for $As_2S_3$.

| | $\bar{\nu}_t$ | $\bar{\nu}_l$ | $\bar{\nu}_p$ | $(\bar{\nu}_t^2+\bar{\nu}_p^2)^{1/2}$ | $e^*/e$ |
|---|---|---|---|---|---|
| $E \parallel c$ | 383 | 386 | 29 | 384 | ••• |
| | 354 | 363 | 70 | 361 | ••• |
| | 311 | 324 | 100 | 327 | 0.34 |
| | 198 | 205 | 49 | 204 | ••• |
| | 159 | 166 | 43 | 165 | ••• |
| | 140 | 148 | 64 | 154 | ••• |
| $E \parallel a$ | 375 | 378 | 39 | 377 | ••• |
| | 345 | 349 | 34 | 347 | ••• |
| | 299 | 327 | 139 | 330 | 0.42 |
| | 181 | 185 | 46 | 187 | ••• |

TABLE IV. TO, LO, and ionic plasma frequencies ($\bar{\nu}$ in cm$^{-1}$), and effective charges, for $As_2Se_3$.

| | $\bar{\nu}_t$ | $\bar{\nu}_l$ | $\bar{\nu}_p$ | $(\bar{\nu}_t^2+\bar{\nu}_p^2)^{1/2}$ | $e^*/e$ |
|---|---|---|---|---|---|
| $E \parallel c$ | 248 | 250 | 22 | 249 | ••• |
| | 217 | 232 | 82 | 232 | 0.35 |
| | 132 | 136 | 34 | 136 | ••• |
| | 105 | 108 | 22 | 107 | ••• |
| | 94 | 97 | 35 | 100 | ••• |
| $E \parallel a$ | 249 | 249 | 8 | 249 | ••• |
| | 224 | 238 | 65 | 233 | 0.26 |
| | 201 | 209 | 75 | 215 | ••• |
| | 132 | 134 | 26 | 134 | ••• |
| | 106 | 108 | 15 | 107 | ••• |

to an eigenvector consisting largely of a *rigid-sublattice motion* in which the arsenic and the chalcogenide sublattice undergo oppositely directed rigid translations (i.e., all As-As and all S-S or Se-Se spacings preserved) against one another. Using the reduced mass $m$ appropriate to the rigid-sublattice eigenvectors, we can (with a further assumption discussed by Zallen *et al.*) estimate the Szigeti effective charge $e^*$ by means of the expression

$$e^* = (\pi\epsilon_\infty m\nu)^{1/2}\, c[3/(\epsilon_\infty + 2)]\,\bar{\nu}_p \ .$$

The results are listed in Tables III and IV: $e^*(\mathrm{As})/e \approx 0.3$–$0.4$ for these vibrations in $As_2S_3$ and $As_2Se_3$, where $e^*(\mathrm{As})$ is the effective charge applicable to the displacement of each As atom. (The effective charge for the chalcogen atom displacements is two-thirds as large.)

## IV. RELATIONSHIP BETWEEN CRYSTAL AND LAYER SYMMETRIES

### A. Crystal Symmetry and Selection Rules

The four factor-group operations of the $P2_1/n$ ($C_{2h}^5$) crystal space group have been described in Sec. IB and illustrated in Fig. 1(b). The character table for the isomorphic point group ($2/m$) is contained in Table V. All of the irreducible representations (IR's) of this low-symmetry group are one dimensional; there are no symmetry-induced vibrational degeneracies.

The symmetries[18] of the long-wavelength $q \approx 0$ phonons are determined by the factor-group representation generated by the displacements of the atoms in the unit cell; this representation is customarily denoted by $\Gamma$.[20,21] For the 20-atom unit cell of the orpiment crystal structure, $\Gamma$ is 60 dimensional and is, of course, reducible. The characters for $\Gamma$ are given in the fifth row of Table V: Since no atoms lie on crystal symmetry elements, the traces vanish except for the identity. The reduction of $\Gamma$ into IR's is given in the fifth column.

Also listed in Table V is the three-dimensional polar-vector representation $P$, which provides the symmetries of the three zone-center acoustic phonons as well as the selection rules for infrared activity. The reduction of $P$ into IR's, given in column six, specifies the acoustic-mode symmetries, so that the IR's of the 57 optical modes are contained in $\Gamma - P$: $15A_g + 15B_g + 14A_u + 13B_u$. For one-phonon optical absorption a mode must induce a first-order electric moment $p$, so that it necessarily transforms as a vector component. The infrared-active optical modes are therefore those of symmetry types common to $\Gamma - P$ and $P$; the IR's contained in this intersection are $A_u$ and $B_u$. The $A_u$-symmetry optical modes interact with light polarized parallel to the $b$ axis, the $B_u$ modes interact with light polarized in the $ac$ plane.

A Raman-active vibration induces a first-order modulation in the optical-frequency dielectric polarizability, so that it must transform as a component of a symmetric second-rank tensor. The Raman selection rules for $C_{2h}$ symmetry are given in the last column of Table V. The $A_g$ and $B_g$ modes are Raman active.

The mutual exclusion between Raman and infrared activity revealed in Table V is a consequence of the inversion operation contained in the crystal factor group. The presence of the centers of symmetry, which are located on the midplanes between layers and which transform one layer into another, guarantees the division into even ($A_g$ and $B_g$, Raman-allowed, infrared-forbidden) and odd ($A_u$ and $B_u$, Raman-forbidden, infrared-allowed) symmetry types.

The implications of the crystal-symmetry selection rules for our optical experiments can now be spelled out. There are two main points: the number of fundamentals anticipated in the reststrahlen spectra, and the relationship between the observed infrared and Raman frequencies.

The observed reststrahlen spectra of Figs. 2 and 3 are for incident light polarized in the plane of the layer: $E \parallel c$ and $E \parallel a$. Table V shows that the vibrations of $B_u$ symmetry are infrared allowed for

TABLE V. Crystal symmetry and selection rules for zone-center phonons in $As_2S_3$ and $As_2Se_3$.

| Representation | | Class characters | | | | Zone-center modes | | | Selection rules | |
|---|---|---|---|---|---|---|---|---|---|---|
| | | 1 | $\bar{1}$ | $2_b$ | $\bar{2}_b$ | All $\Gamma$ | Acoust. $P$ | Opt. $\Gamma - P$ | Infrared | Raman |
| Irred. reps. | $A_g$ | 1 | 1 | 1 | 1 | 15 | 0 | 15 | ··· | $\alpha_{aa}, \alpha_{bb}, \alpha_{cc}, \alpha_{ac}$ |
| | $B_g$ | 1 | 1 | −1 | −1 | 15 | 0 | 15 | ··· | $\alpha_{ab}, \alpha_{cb}$ |
| | $A_u$ | 1 | −1 | 1 | −1 | 15 | 1 | 14 | $p_b$ | ··· |
| | $B_u$ | 1 | −1 | −1 | 1 | 15 | 2 | 13 | $p_{a \text{ or } c}$ | ··· |
| Unit cell rep. | $\Gamma$ | 60 | 0 | 0 | 0 | | | | | |
| Vector rep. | $P$ | 3 | −3 | −1 | 1 | | | | | |

these polarizations. It is important to note that while each individual $B_u$ vibration is permitted an electric dipole moment in the *ac* plane, its orientation within that plane is *not* specified by symmetry. The vibration-induced dipoles of the 13 $B_u$ modes may lie at all angles with respect to the *a* and *c* axes, so that it is, in principle, possible for all 13 to appear in both polarizations. For any moment to lie nearly parallel to, say, the *c* axis, and to be therefore absent from the $E \parallel a$ reststrahlen spectrum, would be accidental, and not a consequence of crystal symmetry. We would therefore expect, in the context of the crystal symmetry, nearly 13 reststrahlen bands showing up both for $E \parallel a$ and $E \parallel c$.

The Raman-infrared mutual exclusion implied by the crystal symmetry means that there is no symmetry-induced coincidence between frequencies observed in the infrared and Raman spectra. This lack of correlation between the two sets of experimental frequencies is a highly important prediction of the crystal symmetry since, as we shall see, it is in qualitative contradiction with the consequences of the layer symmetry (and with the experimental results).

We defer the comparison of our experimental results to the expectations based on crystal symmetry until after the introduction, in Sec. IV B, of the differing predictions of the layer symmetry.

### B. Layer Symmetry and Selection Rules

Their properties reveal that these crystals behave (to a degree of approximation which we intend to quantitatively characterize) as an assembly of nearly isolated weakly interacting molecular layers. Let us now derive a set of selection rules for these materials from the molecular viewpoint, i.e., in the limit of noninteracting layers. In Sec. I B we introduced the symmetry of the isolated layer, illustrating the factor-group operations in Fig. 1. Before deriving the lattice-vibrational effects of this symmetry in an analysis paralleling that of Sec. IV A, it is necessary to point out that the space group for the layer symmetry is quite different from the space groups to which we are accustomed; it is *not* one of the 230 three-dimensional space groups. The molecular layer of the orpiment structure is a three-dimensional entity, as is obvious from Fig. 1(b). The existence of the dimension normal to the layer plane is recognized within the factor group by the inclusion of the screw-axis operation $2_c$ and the glide-plane operation $\bar{2}_b$, both of which are symmetry operations occuring in the 230 three-dimensional space groups but forbidden to the 17 two-dimensional space groups. However the *translational* symmetry of the layer space group is confined to *two dimensions*, there is no periodicity perpendicular to the layer.

TABLE VI. Number of *m*-periodic space groups in *n*-dimensional space.

| Periodicity dimensions | Dimensionality of space 1 | 2 | 3 |
|---|---|---|---|
| 1 | 2 | 7 | ∞ |
| 2 | ••• | 17 | 80 |
| 3 | ••• | ••• | 230 |

The space group we are dealing with here is a *diperiodic group in three dimensions*. There are 80 such diperiodic space groups, and their properties have been recently treated by Wood.[22] In Table VI we have placed this set of groups in relation to the more familiar group sets in one, two, and three dimensions.

We have determined that the diperiodic group appropriate to the molecular layer in $As_2S_3$ and $As_2Se_3$ is, in Wood's listing, DG32. The space-group symbol is $Pnm2_1$, and the analogous triperiodic-group Schoenflies symbol is $C_{2v}^7$.[22,23] Thus the layer symmetry is orthorhombic, rather than monoclinic like that of the crystal.

A group-theoretical analysis of the symmetry types and selection rules for the layer vibrations is presented in Table VII. Since it follows the lines of that given in Table V for the crystal vibrations, we can quickly proceed to the conclusions and to the differences from the crystal-symmetry results. The layer unit cell contains 10 atoms, so that the unit-cell representation $\Gamma$ is now 30 dimensional. There are 27 nondegenerate optical modes of symmetries given by $\Gamma - P = 7A_1 + 7A_2 + 7B_1 + 6B_2$. Of primary importance to our experiments are the following predictions of the layer-symmetry selection rules: (i) The 7 $A_1$ layer fundamentals are infrared allowed for $E \parallel c$; (ii) the 6 $B_2$ fundamentals are infrared allowed for $E \parallel a$; and (iii) both the $A_1$ and the $B_2$ modes are also Raman active. The presence of vibrations entitled to appear in both Raman and infrared spectra is permitted by the absence of inversion symmetry in the layer factor group.

The critical difference between these results and those of Sec. IV A is in the expected relationship between the infrared and the Raman data. The layer symmetry calls for the appearance in the Raman scattering of the same eigenfrequencies occuring in infrared absorption, in marked contrast to the mutual exclusion dictated by the crystal symmetry (for which any Raman-infrared frequency coincidence would have to be accidental and not symmetry induced). The other major difference is that while both group-theoretical analyses allow 13 fundamentals to appear in the reststrahlen spectra for incident light polarized in the *ac* plane, the layer symmetry requires a separation into independent

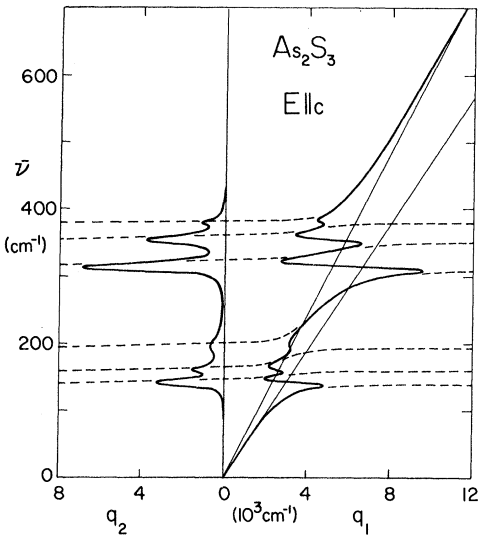


FIG. 10. Polariton dispersion curves for crystalline $As_2S_3$: the $A_1$ modes.

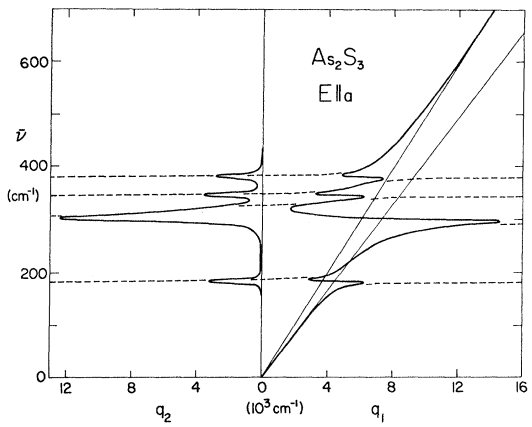


FIG. 11. Polariton dispersion curves for crystalline $As_2S_3$: the $B_2$ modes.

spectra for $E \parallel c$ (seven reststrahlen bands) and $E \parallel a$ (the other six bands), while the crystal symmetry does not (all or most of the 13 bands may appear in a given polarization in the plane).

The final preparation for comparison of the symmetry predictions with our experimental results is the development of a compatibility relationship connecting the two symmetries; this is done in Sec. IV C.

### C. Layer-Crystal Compatibility Relations

In order to understand the actual situation for crystalline $As_2S_3$ and $As_2Se_3$, it is necessary to apply both of the symmetries of Secs. IV A and IV B to the experimental results. While the "correct" symmetry types and selection rules for the lattice vibrations must, of course, be those of the crystal symmetry, the integrity of the molecular layer in these materials makes it essential to take cognizance of the layer symmetry in order to render the data sensible. In this section we make explicit the relationship between the two sets of symmetry predictions; more specifically, we describe the way in which the consequences of crystal symmetry are significantly altered by the superposition of effects of the layer symmetry.

Because the crystal unit cell is two layers thick, there are twice as many normal modes for the crystal (60) than for the layer (30). In the limit of vanishing interaction between layers, the 60 crystal vibrations collapse to 30 degenerate doublets, each pair corresponding to a single layer vibration with adjacent layers vibrating with equal or opposite phase. Turning on the weak interlayer interaction lifts these degeneracies; the result is a set of closely spaced doublets. We need to know the correspondence between the symmetry types of the layer modes and of the derived pairs of crystal modes.

The point groups isomorphic to the layer and crystal factor groups are, respectively, $C_{2v}$ and $C_{2h}$; both are of order 4. Since the monoclinic crystal symmetry is not a subgroup of the orthorhombic layer symmetry, their relationship is not

TABLE VII. Layer symmetry and selection rules for the diperiodic molecular unit.

| Representation | | Class characters | | | | Zone-center modes | | | Selection rules | |
|---|---|---|---|---|---|---|---|---|---|---|
| | | 1 | $2_c$ | $\bar{2}_a$ | $\bar{2}_b$ | All $\Gamma$ | Acoust. $P$ | Opt. $\Gamma-P$ | Infrared | Raman |
| Irred. reps. | $A_1$ | 1 | 1 | 1 | 1 | 8 | 1 | 7 | $p_c$ | $\alpha_{aa}, \alpha_{bb}, \alpha_{cc}$ |
| | $A_2$ | 1 | 1 | −1 | −1 | 7 | 0 | 7 | ... | $\alpha_{ab}$ |
| | $B_1$ | 1 | −1 | 1 | −1 | 8 | 1 | 7 | $p_b$ | $\alpha_{bc}$ |
| | $B_2$ | 1 | −1 | −1 | 1 | 7 | 1 | 6 | $p_a$ | $\alpha_{ac}$ |
| Unit-cell rep. | $\Gamma$ | 30 | 0 | 2 | 0 | | | | | |
| Vector rep. | $P$ | 3 | −1 | 1 | 1 | | | | | |

analogous to that applicable to, say, the crystal field splitting of a spherically symmetric atomic state. The two groups do, however, have in common a subgroup of order 2, which consists of the identity and the glide plane $\overline{2}_b$. The isomorphic point group for the subgroup is $C_s$. The $2\times 2$ character table of this subgroup is contained twice over in both Table V and Table VII, and provides the key to the compatibility relations specifying the pair of crystal IR's derived from each layer IR. The deduced relations are represented in Fig. 14 in a schematic energy-level diagram. Except for the placing of the acoustic modes at zero frequency, the ordering of vibrational frequencies shown in the compatibility diagram is arbitrary.

We will use the totally symmetric $A_1$ optical modes of the layer to illustrate what happens with the inception of intermolecular interaction; this is indicated in the top part of Fig. 14. Each crystal doublet consists of one symmetric (gerade) and one antisymmetric (ungerade) combination, with respect to inversion, of a given layer vibration; for each $A_1$ layer mode, the corresponding crystal modes have $A_g$ and $B_u$ symmetry, respectively. Selection rules for the various symmetries are shown in parentheses on the figure. In the present case, the parent $A_1$ vibration is both Raman and infrared active, while one of the daughter vibrations is Raman active only and the other infrared active only. The infrared-active component is allowed

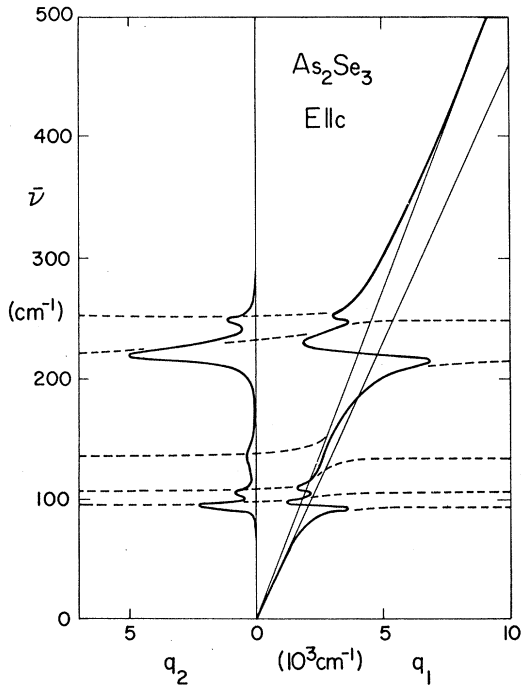


FIG. 12. Polariton dispersion curves for crystalline $As_2Se_3$: the $A_1$ modes.

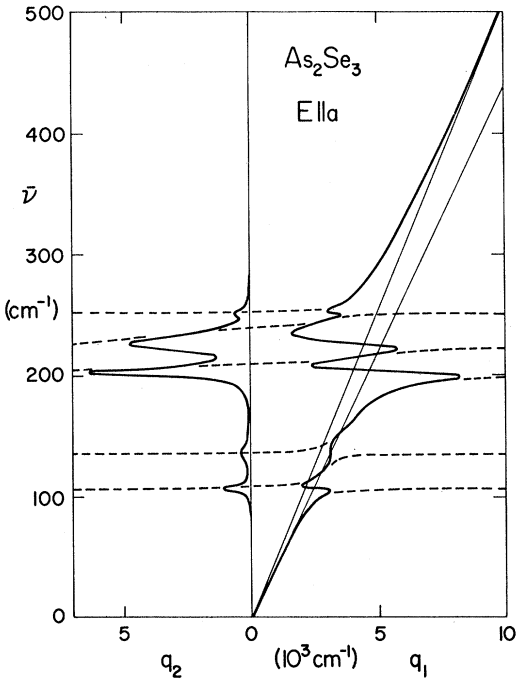


FIG. 13. Polariton dispersion curves for crystalline $As_2Se_3$: the $B_2$ modes.

for any polarization in the *ac* plane, but since the interlayer interaction is weak, we may expect this $B_u$ mode to respect its parentage and to be almost entirely polarized parallel to *c*. Thus the seven $A_1$ optical modes of the layer give rise to seven Raman-infrared doublets, seven near-coincidences between frequencies observed in Raman scattering and in the reststrahlen spectrum for $E \parallel c$.

For the six $B_2$-symmetry layer vibrations an analogous conclusion obtains, viz., six Raman-infrared doublets, this time with the infrared-active $B_u$-symmetry components anticipated in the $E \parallel a$ spectrum.

The $A_2$ and $B_1$ optical modes of the layer give rise to 14 crystalline eigenfrequencies allowed in Raman scattering, and none allowed in reststrahlen for $E \parallel c$ and $E \parallel a$. In addition, as indicated in the bottom part of the compatibility diagram, there are also three low-lying Raman-active modes derived from the layer acoustic modes. We expect these to be largely rigid-layer motions: two shear modes and one rigid beating of adjacent layers against each other along their normal.

## V. INTERLAYER INTERACTIONS AND INTERCRYSTAL SCALING

### A. Interlayer-Interaction Davydov Splittings

For both of the layer crystals investigated here, a set of Raman-infrared doublets has been observed which is in fine agreement with the predictions of Fig. 14. In Table VIII we have compared a dozen

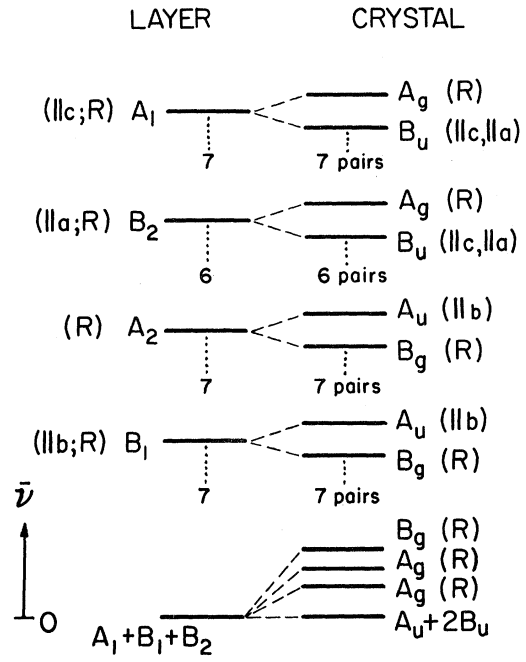


FIG. 14. Compatibility diagram relating the layer and crystal vibrations of the arsenic chalcogenides.

eigenfrequencies observed in Raman scattering with a like number seen in reststrahlen for $E \parallel c$. For each crystal the correlation is striking; the frequency differences, when experimentally discernible, are of the order of a few $cm^{-1}$. This table gives clearcut evidence of the dominance of the layer symmetry, and vindicates the interlayer weak-coupling approach used in the construction of Fig. 14. If the situation corresponded to the strong-coupling case, then the vestiges of the molecular symmetry would be obliterated and the crystal symmetry, in which no Raman-infrared correlation is dictated, would apply. Table VIII convincingly contradicts this.

Following the analysis of Sec. IV, all of the frequencies of Table VIII are assigned to vibrations derived from $A_1$-symmetry layer modes; the crystal symmetries are $A_g$ and $B_u$ for the Raman and infrared frequencies, respectively. The polarization-dependent Raman spectra obtained for $As_2S_3$, such as those of Fig. 5, support these assignments. The $As_2S_3$ Raman lines listed in the table appeared most intensely in polarizations corresponding to diagonal elements ($\alpha_{aa}$ and $\alpha_{cc}$) of the Raman-scattering tensor, in agreement with the selection rules of Tables V and VII for $A_1$ and $A_g$ modes.

Since our infrared measurements have also located lattice fundamentals active for $E \parallel a$, we would would expect another set of $A_g$-$B_u$ Raman-infrared doublets corresponding, this time, to $B_2$-symmetry layer vibrations as shown in Fig. 14. Our data on these doublets are much less complete than for the $A_1$ pairs, possibly because the Raman-active components of the $B_2$ pairs occur for off-diagonal elements (e.g., $\alpha_{ac}$) of the Raman-scattering tensor (Table V), for which our experiments are less sensitive. For $As_2S_3$, the $A_g$ vibration corresponding to the $B_2$-derived $B_u$ mode at 299 $cm^{-1}$ (seen strongly in reststrahlen for $E \parallel a$) has been located at 293 $cm^{-1}$. The $\alpha_{ac}$ polarization of the strong 293-$cm^{-1}$ Raman line is clearly exhibited in Fig. 5. For $As_2Se_3$, an intense $B_2$ doublet is observed at 201-202 $cm^{-1}$, and a pair of weak Raman-infrared ($\parallel a$) lines is also seen at 146-142 $cm^{-1}$.

In about one-half of the cases given above and in Table VIII, the $A_g$-$B_u$ frequency differences, though small, are outside of experimental error. (The estimated experimental uncertainty in $\bar{\nu}$ is $\pm 2$ $cm^{-1}$ for the infrared data, $\pm 1$ $cm^{-1}$ for the Raman data.) The $A_g$-$B_u$ splittings of the $A_1$ (or $B_2$) doublets are induced by the vibrational interaction between molecular layers. Splittings such as these, in which the degeneracy of corresponding excitations on a set of equivalent (in the context of the crystal-symmetry factor group) molecules is lifted by their mutual interaction, are well known for molecular crystals and crystals containing complex ion groups with their own internal vibrations.[24] Referred to as either Davydov or factor-group or correlation field splittings, they are simply the classical frequency differences between normal modes of a lattice of coupled oscillators. (These are to be distinguished from crystal field splittings, in which molecular degeneracies are lifted by the low symmetry of the crystalline environment.[25] Since all the layer vibrations are nondegenerate, there are no crystal field splittings in $As_2S_3$ and $As_2Se_3$.) The term factor-group splitting derives from the fact that the group-theoretical application of the crystal factor group (as in Sec. IV A) automatically incorporates the splittings. The use of this term would be ambiguous here because, for layer crystals, the "molecular" symmetry is another factor group, that of the diperiodic space group. We will employ the term Davydov splitting in our discussion, although

TABLE VIII. Raman-infrared Davydov doublets ($\bar{\nu}$ in $cm^{-1}$) for $As_2S_3$ and $As_2Se_3$. These are $A_g$-$B_u$ pairs derived from $A_1$-symmetry layer vibrations.

| $As_2S_3$ | | $As_2Se_3$ | | |
|---|---|---|---|---|
| Infrared $E \parallel c$ | Raman $\alpha_{aa}, \alpha_{cc}$ | Infrared $E \parallel c$ | Raman $\alpha_{aa}, \alpha_{cc}$ | $\bar{\nu}(As_2Se_3)/\bar{\nu}(As_2S_3)$ |
| 383 | 382 | 268 | 273 | 0.71 |
| 354 | 355 | 248 | 248 | 0.70 |
| 311 | 311 | 217 | 216 | 0.70 |
| 198 | 204 | 132 | 132 | 0.66 |
| 159 | 154 | 105 | 104 | 0.67 |
| 140 | 136 | 94 | 90 | 0.66 |

a more descriptive terminology would be intermolecular-interaction splitting or interlayer-interaction splitting.

The two members of each Davydov doublet in $As_2S_3$ and $As_2Se_3$ occur in separate spectra. A layer vibration possessing both Raman and infrared activity gives rise to two crystalline offspring with one inheriting all the Raman strength and the other all the infrared strength. For the crystal vibration composed of the even-symmetry (inversion-invariant) combination of vibrations on adjacent layers, the electric moments of adjacent layers are antiparallel and cancel out while the Raman-tensor components add. For the odd-symmetry (reversal under inversion) crystal vibration, the electric moments add while the Raman components cancel. Thus the Davydov splittings are inaccessible in a single experiment, and must be attacked with a combination of Raman scattering and infrared absorption, as done here.

The largest of the optical-phonon Davydov splittings observed is 6 $cm^{-1}$ for $As_2S_3$, and 5 $cm^{-1}$ for $As_2Se_3$. Expressed as a fraction of the total (i.e., molecular) frequency, the rms splitting for the data of Table VIII is about 2% for both crystals and about 4% for the lowest-frequency modes. In the simplest model for a pair of weakly coupled identical oscillators, the frequencies of a split doublet are of the form $(\bar{\nu}_0^2 \pm \Delta^2)^{1/2}$, where $\bar{\nu}_0$ is the isolated-oscillator frequency and $\Delta^2$ is proportional to the coupling force constant. This expression is roughly consistent with the trend of increasing splitting with decreasing $\bar{\nu}_0$ indicated by the data, and with a value of $\Delta$ of the order of 20–30 $cm^{-1}$.

The bottom part of Fig. 14 shows that the effect of the interlayer-interaction Davydov splitting on the rigid-layer motions is to generate three low-lying even-symmetry Raman-active modes for which the odd-symmetry counterparts are at $\bar{\nu} = 0$, the acoustic modes. The frequencies of these modes should directly reflect the size of the interlayer coupling constant $\bar{\nu} \approx \Delta$. Our Raman-scattering measurements on $As_2S_3$ permitted us to observe lines within 10–15 $cm^{-1}$ of the laser frequency. As seen in Figs. 4 and 5, we observe two low-lying Raman lines at 25 and 36 $cm^{-1}$. These are likely candidates for the rigid-layer vibrations; their frequencies are consistent with the estimate of $\Delta$ obtained from the upper optical-phonon frequencies.

The rough value of $\Delta$ deduced from our data is about a factor of 10 smaller than typical values of $\bar{\nu}_0$. Since $\bar{\nu}_0^2$ is proportional to the force constants within the layer, while $\Delta^2$ is proportional to interlayer force constants, we can conclude that the intermolecular vibrational coupling between layers is about 100 times weaker than the molecular bonding.

The discussion of the preceding paragraphs accounts for nearly all of the observed Raman lines of Figs. 4 and 5; we now address ourselves to the remaining ones. The $As_2S_3$ lines at 61, 69, 107, and 179 $cm^{-1}$ occur for polarizations $\alpha_{ab}$ and $\alpha_{cb}$, indicating, via Tables V and VII, that they are $B_g$ modes derived from $A_2$ and $B_1$ layer vibrations. From Fig. 14, the other member of each Davydov doublet would then be either infrared inactive or active for $E \parallel b$; this would account for their absence from our reststrahlen spectra. Note also that their $\alpha_{ab}$ and $\alpha_{cb}$ polarizations are a likely explanation of the absence of the corresponding $B_g$ modes from our $As_2Se_3$ Raman spectrum; the geometry of Fig. 4(a) discriminates against polarizations involving $b$. In $As_2S_3$ there is a very weak Raman line at 326 $cm^{-1}$, and in $As_2Se_3$ there is a moderately strong one at 231 $cm^{-1}$. These two frequencies are suspiciously close to the LO frequencies of the strongest (largest TO-LO splitting) reststrahlen bands listed in Tables III and IV. The $As_2S_3$ Raman line at 359 $cm^{-1}$ also lines up closely with an LO frequency. The origin of these three lines is, however, unclear, since the LO representative of each infrared-active mode should, like the TO, not appear in Raman scattering.

In a recent paper, Verble and Wieting[26] report the observation of Raman-infrared degeneracy for a pair of vibrations in $MoS_2$, a layer crystal for which (as for $As_2S_3$ and $As_2Se_3$) mutual exclusion would be expected from the crystal symmetry. They conclude that "mode degeneracy will prove to be characteristic of all layer compounds with more than one layer in the unit cell." The results of the present investigation are entirely consistent with the spirit of their statement. Of course, the "degeneracy" is not exact and in the present case we have succeeded in resolving Davydov splittings, in addition to presenting the first analysis of the crucial diperiodic symmetry of the two-dimensionally extended "molecules" making up such crystals.

In general, for a layer crystal with $n$ layers per crystal unit cell, each layer vibration gives rise to a set of $n$ near-degenerate crystal vibrations, i.e., an $n$-fold Davydov multiplet. It should be pointed out that for $n = 2$, the appearance of Raman-infrared Davydov doublets, such as those observed for $As_2S_3$, $As_2Se_3$, and $MoS_2$, depends upon the circumstance that the layer lacks a center of symmetry. For a layer crystal in which the diperiodic symmetry contains the inversion operation (e.g., graphite), the layer vibrations themselves exhibit mutual exclusion and it can be shown that each Davydov doublet includes a silent mode (inactive in both Raman and infrared).

### B. $As_2S_3$-$As_2Se_3$ Scaling Relation

When we presented our Raman spectra for the two crystals in Fig. 4, we displayed them with dif-

ferent frequency scales in order to emphasize their similarities, such as the distinctive set of five lines seen at the high-frequency end of each spectrum. Similar correspondences can also be set up between the reststrahlen spectra, for example, between the strongest bands seen for $E \parallel c$ (311 $cm^{-1}$ for $As_2S_3$, 219 $cm^{-1}$ for $As_2Se_3$). In the last column of Table VIII we have listed values of the intercrystal frequency ratio $r = \bar{\nu}(As_2Se_3)/\bar{\nu}(As_2S_3)$ for corresponding $A_1$ vibrations of the two layer crystals. (The ratio is taken using the average frequency for each Davydov doublet.) We unexpectedly obtain a tantalizingly simple result: To a close approximation, the frequency spectra of the two materials are related by a simple scaling factor.

For the $A_1$-vibration data of Table VIII, the mean value of $r$ is 0.68, and the rms deviation among the six values shown is 0.02. Though slightly less complete, an analogous set of ratios for $B_2$ vibrations can be obtained by comparing reststrahlen spectra for $E \parallel a$. Five $B_2$ correspondences are found: For these the mean value of $r$ is 0.73, and the rms deviation is 0.02. While the difference between the two mean values may be significant, we have combined both sets of data into one to yield $r = 0.70$ with an rms deviation of 0.03. (A scale factor of 0.70 was employed in Fig. 4.)

Such a simple scaling relation between lattice frequencies is not readily anticipated for two complex crystals, even if their structures are, as here, intimately related. This is because each eigenfrequency depends sensitively upon the shape of the mode, i.e., the vibrational eigenvector. The close adherence to a constant $r$ is a strong indication that almost identical eigenvectors occur in crystalline $As_2S_3$ and $As_2Se_3$. This is striking confirmation of the extremely close isomorphicity of the two crystals.

We can attempt to interpret the scaling factor of 0.70 in terms of the different masses and force constants of $As_2S_3$ and $As_2Se_3$. Assume that $\bar{\nu} \sim (k/\mu)^{1/2}$, where $\mu$ is the effective reduced mass and $k$ the effective force constant for the mode. Then $r$ becomes equal to the product of $[k(As_2Se_3)/k(As_2S_3)]^{1/2}$ and $[\mu(As_2Se_3)/\mu(As_2S_3)]^{-1/2}$. To obtain a representative reduced-mass ratio we use the rigid-sublattice modes discussed in Sec. III C; the result for $[\mu(As_2Se_3)/\mu(As_2S_3)]^{-1/2}$ is 0.80. Thus the mass difference accounts for most of the scaling factor, with the remaining factor of 0.70/0.80 indicating that force constants in $As_2Se_3$ are smaller, by approximately 25%, than those in $As_2S_3$.

We close with a comparison of our results to Raman and reststrahlen spectra reported for the bulk glasses, amorphous $As_2S_3$ and $As_2Se_3$. Raman experiments on the amorphous forms have been performed by Ward.[3] A broad Raman band is observed in each glass in the frequency region in which the dominant lines occur in the crystal: The band is centered at about 340 $cm^{-1}$ in $a$-$As_2S_3$ and about 230 $cm^{-1}$ in $a$-$As_2Se_3$. A single broad reststrahlen band also dominates the infrared spectrum of each glass. Felty *et al.*[2] have analyzed their reflectivity spectra to derive an oscillator frequency of 300 $cm^{-1}$ for $a$-$As_2S_3$ and 217 $cm^{-1}$ for $a$-$As_2Se_3$. These frequencies are close to those of the infrared-dominant rigid-sublattice modes we have found in the crystals: 299 and 311 $cm^{-1}$ for $As_2S_3$ and 217 and 224 $cm^{-1}$ for $As_2Se_3$. This indicates that the infrared-active vibrations in the glasses are predominantly of this rigid-sublattice character, with each arsenic atom vibrating oppositely to its three neighboring sulfur or selenium atoms, and each sulfur or selenium atom vibrating oppositely to its two neighboring arsenic atoms. Finally, we note that essentially the same $As_2S_3$-$As_2Se_3$ scaling ratio is observed for the glasses as for the crystals. The ratio of Raman frequencies is 0.68 and that of infrared frequencies is 0.72; both are in fine agreement with the crystalline consensus of $0.70 \pm 0.03$.

## VI. SUMMARY

An experimental investigation of the long-wavelength lattice vibrations of crystalline $As_2S_3$ and $As_2Se_3$ has been carried out by means of their interaction with light. The reststrahlen spectra of Figs. 2 and 3 have been analyzed to obtain the TO, LO, and ionic plasma frequencies, as well as the effective charges, of Tables III and IV. In addition to the standard dielectric dispersion properties, the infrared data have yielded the polariton dispersion curves of Figs. 10–13.

The lattice-vibrational consequences of both the crystal symmetry and the unusual diperiodic symmetry of the individual layer have been group-theoretically deduced. This analysis, the results of which are depicted in Fig. 14, reveals that the effects of the interlayer interactions, the vibrational Davydov splittings, must be attacked with a *combination* of infrared and Raman experiments; the two members of each Davydov doublet never appear together in the same spectrum. This was our main application for the Raman spectra of Figs. 4 and 5. Striking evidence for the dominance of the layer symmetry, along with information about the strength of the weak interaction between layers, has been provided by the Raman-infrared Davydov doublets listed in Table VIII.

A surprisingly simple scaling relation has been found to connect corresponding lattice frequencies of the two crystals: $\bar{\nu}(As_2Se_3)/\bar{\nu}(As_2S_3) = 0.70 \pm 0.03$. The scaling factor is only partially accounted for by the difference in masses, indicating that force

constants in $As_2Se_3$ are smaller than in $As_2S_3$. Finally, comparison of the lattice spectra of the crystals to those of the corresponding glasses has yielded insight into the nature of the dominant vibrations of the amorphous forms.

ACKNOWLEDGMENTS

The authors are indebted to R. C. Keezer, P. J. Vernon, and C. H. Griffiths for providing synthetic crystals of $As_2Se_3$, and have benefitted from discussions with H. Scher, P. Goldstein, and R. S. Knox.

[1]A. R. Hilton, J. Non-Cryst. Solids 2, 28 (1970); B. T. Kolomiets, T. F. Mazets, Sh. M. Efendiev, and A. M. Andriesh, *ibid.* 4, 45 (1970); F. Kosek and J. Tauc, Czech. J. Phys. B 20, 94 (1970); J. Tauc, A. Menth, and D. L. Wood, Phys. Rev. Letters 25, 749 (1970).

[2]E. J. Felty, G. Lucovsky, and M. B. Myers, Solid State Commun. 5, 555 (1967).

[3]A. T. Ward, J. Phys. Chem. 72, 4133 (1968).

[4]Some preliminary results of the infrared experiments were briefly presented in M. L. Slade and R. Zallen, Bull. Am. Phys. Soc. 14, 301 (1969); M. L. Slade, R. Zallen, and R. C. Keezer, *ibid.* 14, 740 (1969).

[5]N. Morimoto, Mineral. J. (Sapporo) 1, 160 (1954).

[6]A. A. Vaipolin, Kristallografiya 10, 596 (1965) [Sov. Phys. Crist. 10, 509 (1966)].

[7]B. L. Evans and P. A. Young, Proc. Roy. Soc. (London) A297, 230 (1967).

[8]The intralayer bond length for $As_2S_3$ closely matches the sum of Pauling's (Ref. 9) covalent radii for As and S; for $As_2Se_3$ the bond length is about 4% larger than the corresponding sum of covalent radii.

[9]L. Pauling, *The Nature of Chemical Bond* (Cornell U. P., Ithaca, N. Y., 1960).

[10]The assumption of van der Waals forces is usually made in the absence of better information and is an admission of ignorance about the detailed nature of the intermolecular interaction. Actually for both $As_2S_3$ and $As_2Se_3$ the interlayer atomic separations are 7–8% smaller than the sums of Pauling's (Ref. 9) van der Waals radii, so that the interlayer bonding is somewhat stronger than van der Waals and probably contains an admixture of weak covalent bonding.

[11]D. L. Greenaway, G. Herbeke, F. Bassani, and E. Tosatti, Phys. Rev. 178, 1340 (1969).

[12]*International Tables for X-Ray Crystallography, Symmetry Groups* (Kynoch, Birmingham, England, 1952), Vol. 1.

[13]R. W. G. Wyckoff, *Crystal Structures* (Wiley, New York, 1963), Vol. 1.

[14]Orpiment samples were obtained from Ward's Natural Science Establishment, Rochester, N. Y.

[15]The room-temperature band gap is about 1.9 eV for crystalline $As_2Se_3$ (Refs. 16 and 17) and 2.7 eV for crystalline $As_2S_3$ (Refs. 7 and 17).

[16]R. F. Shaw, W. Y. Liang, and A. D. Yoffe, J. Non-Cryst. Solids 4, 29 (1970).

[17]R. E. Drews, R. Zallen, and R. C. Keezer, Bull. Am. Phys. Soc. 13, 454 (1968).

[18]We specify $q \approx 0$ rather than $q = 0$ because of the complication, for infrared-active phonons, of photon-phonon interaction for $q$'s of the order of $\omega/c$. By $q \approx 0$ we mean wave vectors small compared to the Brillouin-zone dimensions ($q \ll \pi/a$) but large compared to the range of polariton effects ($q \gg \omega/c$). The symmetries (IR's) and degeneracies determined by the full crystal (or layer) symmetry strictly apply only at $q = 0$, where the infrared-active phonons are represented by the LO modes. We ignore the lowered symmetry away from $q = 0$ and assume that the same IR's and degeneracies apply, aside from TO-LO splittings, to $q \approx 0$ phonons.

[19]K. Huang, Proc. Roy. Soc. (London) A208, 352 (1951); M. Born and K. Huang, *Dynamical Theory of Crystal Lattices* (Oxford U. P., London, 1954); J. J. Hopfield, Phys. Rev. 112, 1555 (1958); E. Burstein, Comments Solid State Phys. 1, 202 (1969).

[20]R. Zallen, G. Lucovsky, W. Taylor, A. Pinczuk, and E. Burstein, Phys. Rev. B 1, 4058 (1970).

[21]A. S. Barker, Jr., Phys. Rev. 132, 1474 (1963); 135, A742 (1964); S. H. Chen, *ibid.* 163, 532 (1967); R. Zallen, *ibid.* 173, 824 (1968).

[22]E. A. Wood, Bell System Tech. J. 43, 541 (1964); Bell Telephone System Tech. Publ. Monographs 4680, 1964 (unpublished).

[23]Some care is required in specifying the correspondences between symmetry axes of DG32, $C_{2v}^7$, and $C_{2h}^5$. We sidestep notational complications here by always referring, in our group-theoretical tables, to the set of axes defined by Fig. 1.

[24]D. F. Hornig, J. Chem. Phys. 16, 1063 (1948); A. S. Davydov, Zh. Eksperim. i Teor. Fiz. 18, 210 (1948); H. Winston and R. S. Halford, J. Chem. Phys. 17, 607 (1949); R. M. Hexter, *ibid.* 33, 1833 (1960); L. C. Kravitz, J. D. Kingsley, and E. L. Elkin, *ibid.* 49, 4600 (1968).

[25]R. S. Halford, J. Chem. Phys. 14, 8 (1946).

[26]J. L. Verble and T. J. Wieting, Phys. Rev. Letters 25, 362 (1970). Verble and Wieting refer to rigid-layer modes, such as those we assign to the low-lying Raman lines of $As_2S_3$, as "quasiacoustical" modes; they have not yet observed these for $MoS_2$.